HHS Public Access

Author manuscript

Neuron. Author manuscript; available in PMC 2023 January 05.

Published in final edited form as:

Neuron. 2022 January 05; 110(1): 86–95.e5. doi:10.1016/j.neuron.2021.10.006.

Structural mechanisms of assembly, permeation, gating, and pharmacology of native human rod CNG channel

Jing Xue[1,2], **Yan Han**[1,2], **Weizhong Zeng**[1,2], **Youxing Jiang**[1,2,*]

[1]Howard Hughes Medical Institute and Department of Physiology, University of Texas Southwestern Medical Center, Dallas, Texas, USA

[2]Department of Biophysics, University of Texas Southwestern Medical Center, Dallas, Texas, USA

Summary

Mammalian cyclic nucleotide-gated (CNG) channels are non-selective cation channels activated by cGMP or cAMP and play essential roles in the signal transduction of the visual and olfactory sensory systems. CNGA1, the principal component of the CNG channel from rod photoreceptors, can by itself form a functional homotetrameric channel and has been used as the model system in the majority of rod CNG studies. However, the native rod CNG functions as a heterotetramer consisting of three A1 and one B1 subunits and exhibits different functional properties than the CNGA1 homomer. Here we present the functional analysis of human rod CNGA1/B1 heterotetramer and its cryo-EM structures in apo, cGMP-bound, cAMP-bound, and L-cis-Diltiazem-blocked states. These structures, with resolution ranging from 2.6 to 3.3 Å, elucidate the structural mechanisms underlying the 3:1 subunit stoichiometry, the asymmetrical gating upon cGMP activation, and the unique pharmacological property of the native rod CNG channel.

eTOC Blurb:

Xue et al. present the high resolution structures of the human rod CNGA1/B1 heterotetrameric channel in apo, cGMP-bound, cAMP-bound, and L-cis-Diltiazem-blocked states. These structures elucidate the structural mechanisms underlying the subunit stoichiometry, the asymmetrical gating upon cGMP activation, and the unique pharmacological property of the native rod CNG channel.

Keywords

cyclic nucleotide-gated; native rod CNG channel; cGMP and cAMP activation; CNGA1 and CNGB1 heterotetramer; signal transduction; visual and olfactory sensory system

[*]Lead Contact: Youxing Jiang, Ph.D., Department of Physiology, UT Southwestern Medical Center, 5323 Harry Hines Blvd., Dallas, Texas 75390-9040, Tel. 214 645-6027; Fax. 214 645-6042; youxing.jiang@utsouthwestern.edu.

Author contributions: J.X. prepared the samples; Y.H. and J.X. performed data acquisition, image processing, and structure determination; W.Z. performed electrophysiology recording; all authors participated in research design, data analysis, discussion, and manuscript preparation.

Declaration of interests: The authors declare no competing financial interests.

Introduction

Mammalian cyclic nucleotide-gated (CNG) channels play vital roles in the signal transduction of photoreceptors and olfactory sensory neurons (Bradley et al., 2005; Craven and Zagotta, 2006; Finn et al., 1996; Kaupp and Seifert, 2002; Matulef and Zagotta, 2003; Yau and Baylor, 1989; Zagotta and Siegelbaum, 1996). Belonging to the six-transmembrane (6-TM) voltage-gated ion channel superfamily, CNG channels are non-selective tetrameric cation channels activated by cyclic nucleotide rather than voltage. In mammals, the CNG channel family consists of six homologous members: four members in the CNGA subfamily (A1 to A4) and two in the CNGB subfamily (B1 and B3) (Bonigk et al., 1993; Chen et al., 1993; Dhallan et al., 1990; Gerstner et al., 2000; Kaupp et al., 1989). The three principal components of CNG channels, including rod CNGA1, olfactory CNGA2, and cone CNGA3, can by themselves form functional homotetrameric channels in heterologous expression systems and have been commonly used as model systems to characterize the gating and permeation properties of CNG channels (Finn et al., 1996; Kaupp, 1995; Zagotta and Siegelbaum, 1996). However, a native CNG channel functions as a heterotetramer consisting of both CNGA and CNGB subunits (Bradley et al., 1994; Chen et al., 1993; Korschen et al., 1995). In rod photoreceptor, a native CNG channel is assembled by CNGA1 and CNGB1 in 3:1 stoichiometry; in olfactory sensory neurons, a native CNG channel consists of two CNGA2, one CNGA4 and one CNGB1b (an olfactory-specific shorter splice variant of CNGB1) subunits; the stoichiometry of a native cone CNG, consisting of CNGA3 and CNGB3, has not yet be defined unambiguously with both 3:1 and 2:2 having been proposed (Bonigk et al., 1999; Peng et al., 2004; Shuart et al., 2011; Weitz et al., 2002; Zheng et al., 2002; Zheng and Zagotta, 2004; Zhong et al., 2002).

Although members of the CNGB subfamily cannot form functional channels by themselves, they convey distinct functional properties to the native channels (Biel et al., 1999; Finn et al., 1996; Kaupp and Seifert, 2002; Matulef and Zagotta, 2003). In the native rod CNG, the CNGB1 subunit renders the heterotetrameric channel with different ion permeation and gating properties than the CNGA1 homomer. While Ca^{2+} can bind in the filter of CNGA1 homomer with high affinity and block the conduction of monovalent cations, Ca^{2+} blockage becomes much weaker in the native CNG. The native CNG can be fully activated by cGMP and also partially activated by cAMP at higher concentrations. In contrast, the homotetrameric CNGA1 channels are poorly activated by cAMP. The native rod CNG also exhibits a distinct pharmacological property. L-cis-Diltiazem, a stereoisomer of L-type Ca^{2+} channel blocker D-cis-Diltiazem used for treating some cardiovascular diseases, can effectively block the native rod CNG but is a much weaker blocker for the CNGA1 homomer (Chen et al., 1993; Haynes, 1992; Korschen et al., 1995; Shammat and Gordon, 1999). In addition, CNGB1 may also play important roles in the regulation and cellular targeting of the native channel (Chen et al., 1994; Hsu and Molday, 1993; Kizhatil et al., 2009; Korschen et al., 1995; Michalakis et al., 2011; Poetsch et al., 2001; Trudeau and Zagotta, 2003).

Although CNG channels have been extensively studied for many years with a plethora of biochemical and physiological data, the majority of the studies have been focused on the homotetrameric CNG channels formed by the CNGA subunits, including the

recent structural studies of the *C. elegans* CNG channel (TAX-4) and human CNGA1 homotetramer (Li et al., 2017; Xue et al., 2021; Zheng et al., 2020). In the absence of structural information of CNGB subunits, the molecular mechanisms underlying the distinct gating, permeation, and pharmacological properties of native CNG channels remain elusive. To this end, we co-expressed the human rod CNGA1 and CNGB1 subunits, purified the CNGA1/B1 heterotetrameric complex with 3:1 subunit stoichiometry, and determined its structures in multiple states, including the apo closed state, the cGMP-bound open state, the cAMP-bound closed state, and the L-cis-diltiazem-blocked state. These structures allow us to visualize for the first time the structural features that determine the permeation, gating, and pharmacological properties of native rod CNG as well as the 3:1 subunit stoichiometry of channel assembly. Furthermore, the current structural and functional analyses of the CNGA1/B1 heterotetrameric channel provide a framework for future studies of modulation and regulation of the native rod CNG channel.

Results

Biochemistry and Electrophysiology of CNGA1/B1 heterotetramer

A bi-cistronic construct of native human rod CNG channel containing both CNGA1 and CNGB1 genes was cloned into the pEZT-BM expression vector and expressed in HEK293F cells using BacMam system (STAR Methods). By linking the two genes with a sequence of P2A self-cleaving peptide that induces ribosomal skipping during translation (Liu et al., 2017), the expression of the bi-cistronic construct yielded a homogeneous 3:1 complex of CNGA1/B1. The N-terminal 144 residues of CNGA1 and the N-terminal glutamic acid-rich protein domain (GARP, residues 1–455) of CNGB1 were removed in the final protein construct used for structural determination, as the deletion mutation significantly improved the complex expression and stability (Figure S1A).

The pEZT-BM vector containing the bi-cistronic construct of the truncated rod CNG was also used to transfect the HEK293 cells for the functional characterization of the expressed CNGA1/B1 heterotetramer using patch clamp recordings in both whole-cell and inside-out configurations. Three distinct biophysical properties between the CNGA1/B1 heterotetramer and the CNGA1 homotetramer were characterized, namely Ca^{2+} blockage, cGMP and cAMP activation, and L-cis-Diltiazem blocking (Chen et al., 1993; Haynes, 1992; Korschen et al., 1995; Shammat and Gordon, 1999) (Figure 1 and Figure S1B–S1E). Hereafter, the rod CNG heterotetramer and homotetramer will be simply referred to as CNGA1/B1 and CNGA1, respectively. The expressed CNGA1/B1 exhibits a lower affinity of Ca^{2+} blockage with K_i of about 84 μM as compared to K_i of about 4 μM for CNGA1 (Figure 1A and Figure S1B). While cGMP can fully activate both CNGA1 and CNGA1/B1, cAMP only partially activates CNGA1/B1 at high concentrations and barely activates CNGA1 (Figure 1B and Figure S1C). One interesting pharmacological property of rod CNG is that its native form but not the CNGA1 homomer can be effectively blocked by L-cis-Diltiazem. Indeed, L-cis-Diltiazem can block the expressed CNGA1/B1 channel with K_i of about 4 μM but has little effect on the conduction of CNGA1 in our measurements (Figure 1C and Figure S1D). Diltiazem is likely membrane-permeable as it can block the channel by applying from either side of the membrane (Figure S1D–S1E). To ensure that the truncation of CNGA1/B1 does

not significantly alter the biophysical properties of the native channel, we also performed a similar functional characterization of the expressed full-length CNGA1/B1channel, which exhibits similar cGMP activation and Ca^{2+} blockage properties to those of the truncated CNGA1/B1 (Figure S2).

Structure determination of CNGA1/B1

The single particle cryo-EM structures of CNGA1/B1 in various states were determined, including apo, cGMP-bound, cAMP-bound, and L-cis-Diltiazem-blocked states (Figure S3–S6, STAR Methods, and Table S1). The EM density maps of these structures are of high quality for accurate model building for the major part of the channel containing residues 156–605 for the A1 subunit and residues 645–1084 for the B1 subunit (Figure S7). The channel in the apo state appears to be more stable and yields higher resolution structures with better-resolved maps at the cytosolic soluble region. Therefore, the apo CNGA1/B1 will be used for its overall structure description (Figure 2A–2B). The three A1 subunits in CNGA1/B1 are not the same because each A1 has a different pair of neighboring subunits. In addition, the gating conformational changes are also different among the three A1 subunits as will be discussed later. We, therefore, designate the three A1 subunits as $A1_L$, $A1_D$, and $A1_R$, respectively, based on their relative position to the B1 subunit (Left, Diagonal and Right, Figure 2B inset).

The overall structure of the apo CNGA1/B1 is strikingly similar to that of the apo CNGA1. Of the modeled regions in the apo CNGA1/B1 structure, A1 and B1 subunits share about 35% sequence identity and their structures align very well with identical domain arrangement, including the 6-TM transmembrane region that is not domain-swapped, the C-linker domain containing helices A'-F', and the C-terminal cytoplasmic cyclic nucleotide-binding domain (CNBD) containing helices A, P, B, C and a β-roll (β1-β8) (Figure 2C and Figure S8). This high structural homology along with the conservation of key interfacial residues for inter-subunit contacts allows the B1 subunit to seamlessly replace an A1 subunit and form a stable heterotetrameric complex with a high structural similarity to the CNGA1 homomer.

Along the ion conduction pathway, two noticeable differences between A1 and B1 subunits likely contribute to different ion conduction properties between the native rod CNG and CNGA1 homomer (Figure 2D). Firstly, the highly conserved glutamate (Glu365) in the selectivity filter of the A1 subunit becomes a glycine (Gly848) in B1. As the filter glutamate is essential for Ca^{2+} binding within the CNGA1 filter and subsequent block of monovalent currents, its absence in the B1 filter likely contributes to the lower Ca^{2+} blocking affinity in CNGA1/B1. Indeed, when Gly848 was mutated to glutamate in the B1 subunit, the mutant CNGA1/B1 channel exhibits a much higher Ca^{2+} blocking affinity with a K_i of about 5.7 μM, similar to that of CNGA1 homomer (Figure 2E). A control experiment showed the same L-cis-Diltiazem blocking property between the mutant and the wild-type CNGA1/B1, confirming that the mutation in B1 did not interfere with the formation of the heterotetrameric channel (Figure S9). The second interesting feature of the CNGA1/B1 pore is the presence of arginine (Arg880) in the B1 subunit at the cytosolic entrance of the channel, whereas the A1 subunit has a glycine (Gly397) at the equivalent position (Figure

2D). We suspect that this Arginine may modulate the channel conductance by partially blocking the channel. Indeed, replacing R880 with glycine in the B1 subunit yielded a mutant CNGA1/B1 channel with higher single channel conductance (~26 pS) than that of the wild-type CNGA1/B (~15 pS) (Figure 2F).

Structural basis of 3:1 subunit stoichiometry

CNGA1 subunit contains a C-terminal leucine zipper domain (CLZ, residues 623–679) in the post-CNBD region that can by itself form a parallel 3-helix coiled coil and is suggested to be important for determining the 3:1 subunit stoichiometry of the native rod CNG (Shuart et al., 2011). In the structure of apo CNGA1/B1, weak protein density was observed at the region below the ring of CNBD domains. A focused 3D classification by masking around this region yielded an EM map, albeit with a lower overall resolution, that allows us to visualize the density of a long 3-helix coiled coil that matches well with the crystal structure of the isolated CLZ domain, indicating that the CLZs of A1 subunits indeed form a parallel 3-helix coiled coil in CNGA1/B1 channel (Figure 3A–3C and Figure S3). Right underneath the CNGB1 C-helix, we also observe an extra piece of density likely from a helix at the C-terminal part of the B1 subunit. This helix is assigned as D-helix for being right after the C-helix (Figure 3B). The EM density maps of the coiled coil region and the D-helix are not of sufficient quality for unambiguous assignment of the side chains and therefore are only modeled as poly-A helices. The N-terminal part of the D-helix makes direct contact with the coiled coil by leaning against two of the coiled coil helices at about 60° angle (Figure 3B). The coiled coil is not oriented in parallel to the pseudo 4-fold axis of the CNGA1/B1 channel. Instead, its C-terminal end tilts markedly towards the B1 subunit, which is likely caused by its interactions with the D-helix of the B1 subunit.

Consistent with the previous study (Shuart et al., 2011), the structure of CNGA1/B1 would also suggest that the formation of a 3-helix coiled coil by CNGA1 CLZ domain ensures a composition of three A1 subunits in the assembly of a native channel. It was demonstrated that the deletion of CLZ in CNGA1 could lead to the formation of heterotetrameric channels with multiple B1 subunits, such as 2A1:2B1 in addition to 3A1:1B1. When expressed in *Xenopus* oocytes, these CNGA1/B1 heteromers with mixed stoichiometry exhibited different L-cis-Diltiazem blocking and cAMP activation properties than the native CNGA1/B1 with 3:1 stoichiometry. To confirm the suggested role of the CLZ domain, we measured the Ca^{2+} blocking of the mutant CNGA1/B1 with CLZ deletion in the A1 subunit (CNGA1ΔCLZ/B1). As the missing filter glutamate in the B1 subunit contributes to the lower affinity Ca^{2+} blocking in CNGA1/B1, we expect a further decrease of Ca^{2+} affinity if there is an increased population of heteromers containing multiple B1 subunits. Indeed, HEK293 cells expressing CNGA1ΔCLZ/B1 exhibit lower Ca^{2+} blocking affinity (K_i ~161μM) than the cells expressing wild-type CNGA1/B1 (K_i ~84μM) (Figure 3D and Figure S10), consistent with the suggestion that the removal of CLZ increases the population of heterotetramers containing more than one B1 subunits.

Asymmetrical pore opening of CNGA1/B1

The ion conduction pore of CNGA1/B1, consisting of S5s, S6s, and pore (P) helices from both A1 and B1 subunits, adopts a closed conformation in the apo structure and an open

conformation in the cGMP-bound structure (Figure 4A–4D). With high structural homology between A1 and B1 subunits, the apo CNGA1/B1 has a quite symmetrical closed pore similar to that of CNGA1 homomer with a closed gate in the middle of the membrane formed by two layers of conserved hydrophobic residues, including F389s and V393s from A1, and Phe872 and Ile876 from B1 (Figure 4C–4D).

Two open structures, termed open I and open II respectively, were obtained from the 3D classification of the cGMP-bound CNGA1/B1 sample. The two structures adopt different conformations at the CNBD of the B1 subunit but share a similar open ion conduction pore. Thus, we will just use the open I structure to elucidate the pore opening mechanics of CNGA1/B1. Unlike symmetrical CNGA1, the pore opening of CNGA1/B1 is asymmetrical. As shown in the partial structure alignment between the open and closed CNGA1/B1 pores, only two pore-lining S6 helices from $A1_L$ and $A1_D$ subunits undergo outward movement along with rotational motion hinged at Gly385 similar to the opening of CNGA1 (Figure 4C–4D and movie S1). Consequently, the two layers of constriction-forming gating residues from these two S6 helices dilate and rotate away from the central axis. The S6 helices from $A1_R$ and B1 subunits, on the other hand, undergo subtle conformational change upon pore opening and their gating residues remain in a similar position between the open and closed states (Figure 4C–4D). Thus, with unequal movements at S6 helices, the open CNGA1/B1 pore becomes asymmetrical and has a narrower ion conduction pathway than that of the open CNGA1 pore (Figure 4B and 4E). As discussed in the following, this asymmetrical opening of the CNGA1/B1 pore is caused by the interruption of the inter-subunit relay of conformational changes between the B1 subunit and its two neighboring A1 subunits (Figure 5).

Cyclic nucleotide-binding and conformational changes at the gating apparatus

In the cGMP-bound CNGA1/B1 structures, the ligands are present in both A1 and B1 subunits whose CNBDs are conserved and utilize the same set of residues to interact with cGMP in their ligand-binding pockets (Figure 5A). As previously discussed, the two cGMP- bound structures share a similar asymmetrically opened pore but with different conformations at the CNBD of the B1 subunit. While the C-helices in all A1 subunits adopt an activated, up conformation in both structures, the C-helix of the B1 subunit adopts a down conformation similar to that of an apo state despite the presence of ligand in open I structure, but is in an up conformation similar to that of cGMP-bound, activated A1 subunit in open II structure (Figure 5E).

To better understand the difference in cGMP gating between CNGA1/B1 and CNGA1, it is necessary to first review the relay of conformational changes from cGMP binding to channel opening in CNGA1 (Figure 5B–5C): the cGMP binding at CNBD triggers an upward swinging of C-helix closer to the ligand-binding pocket, resulting in an upward translation of helix C’-turn-helix D’ in the C-linker domain; through the inter-subunit elbow-on-shoulder packing between two neighboring C-linkers (Zagotta et al., 2003), the conformational change at helix C’-turn-helix D’ (shoulder) of one subunit propagates to an up and outward movement at helix A’-turn-helix B’ (elbow) of the neighboring subunit; with the tight covalent connection between S6 and helix A’, the elbow movement leads

to pore-opening rotation and dilation of S6 hinged at Gly385 (Figure 5C and movie S2). Thus, the C-helix of an A1 subunit acts like a switch whose upward movement upon cGMP binding is coupled to the pore opening movement of S6 from the neighboring subunit, and all four subunits undergo the same global conformational changes in CNGA1, yielding a symmetrical open pore (Xue et al., 2021).

In a cGMP-activated CNGA1/B1, however, the above described inter-subunit relay of conformation changes from the cytosolic gating apparatus to the pore-lining S6 only occurs between neighboring A1 subunits but is interrupted between B1 and its neighbors ($A1_L$ and $A1_R$), resulting in an asymmetrically opened channel gate with only the S6 helices from subunits $A1_L$ and $A1_D$ adopting an open conformation (Figure 5D–5E and movie S2). The first interruption occurs between $A1_L$ and B1 subunits. While the cGMP-induced conformational changes at the $A1_L$ gating apparatus still propagate to the up and outward movement of helix A'-turn-helix B' elbow in B1 subunit as seen in CNGA1, this B1 elbow movement, however, only translate to dilation but not rotation movement at its S6 helix. Consequently, the S6 gating residues in B1 subunit only translate slightly away from the central axis without any rotation (Figure 5E, left panel). The second disruption occurs between B1 and $A1_R$ subunits. In open I structure, cGMP doesn't induce upward movement at B1 C-helix and its CNBD adopts a conformation similar to the apo state. Consequently, the helix A'-turn-helix B' elbow of $A1_R$ remains static, resulting in the lack of movement at its S6 helix (Figure 5E, middle panel). In the open II structure, even with the B1 C-helix adopting an up and activated conformation, the conformational change at B1 CNBD translates to a smaller up- and outward movement at the $A1_R$ elbow than that observed in the other activated A1 subunits. This reduced elbow movement also fails to translate to any major pore-opening movement at its S6 helix (Figure 5E, right panel). Thus, regardless of the C-helix position in the B1 subunit, the S6 of $A1_R$ makes no or subtle conformational change upon cGMP activation in CNGA1/B1.

In an attempt to reveal the structural basis of cAMP binding and activation in native rod CNG, we also determined the structure of CNGA1/B1 in complex with cAMP. Similar to cGMP, cAMP also binds in both A1 and B1 subunits utilizing the same ligand-binding pocket (Figure 5A). A major difference between the bound cAMP and cGMP is that the purine base adopts anti conformation in cAMP but syn conformation in cGMP. The cGMP guanine base is stabilized to syn conformation by a hydrogen bond between the amino group at its C-2 position and the threonine from CNBD β-roll (Thr562 in A1 and Thr1043 in B1). There is no equivalent amino group in the adenine base of cAMP. The binding of cAMP and cGMP at the same site with different stereochemistry was also observed in the CNBD structures of the HCN2 channel (Zagotta et al., 2003). As expected from the low efficacy of cAMP activation, the cAMP-bound CNGA1/B1 structure remains in a closed conformation and cAMP does not induce any upward movement of C-helices at CNBD of A1 or B1 subunit (Figure S11). This lack of conformational change upon cAMP binding makes it difficult to ascertain the structural mechanism of cAMP activation in CNGA1/B1.

Structural basis of L-cis-Diltiazem blocking

To reveal the structural basis underlying the pharmacological property of the native rod CNG, we also determined the structure of CNGA1/B1 in complex with L-cis-Diltiazem. The complex was prepared in the presence of cGMP as L-cis-Diltiazem is expected to be an open-pore blocker. 3D classification yielded two structures with the clear density of bound blocker in the pore (Figure 6 and Figure S7B). In one structure, CNGA1/B1 adopts the same asymmetrical open conformation as the open I structure with C-helix up in the A1 subunit but down in the B1 subunit. L-cis-Diltiazem binds in the middle of the open pore right below the selectivity filter (Figure 6A–6B). It is interesting to note that the B1 subunit does not provide any specific interaction with the blocker. Instead, L-cis-Diltiazem blocking in the native rod CNG but not in CNGA1 homomer is attributable to the asymmetrical gating of the heterotetrameric channel, in which only two gate-forming phenylalanines (Phe389s from $A1_L$ and $A1_D$) adopt an open conformation, whereas the other two (Phe389 from $A1_R$ and Phe872 from B1) remain in a closed conformation. Consequently, this asymmetrically opened gate creates a perfect open space for L-cis-Diltiazem whose binding is stabilized by van der Waals interactions with surrounding hydrophobic residues ((Figure 6A–6B and Movie S3).

Interestingly, the other L-cis-Diltiazem-bound CNGA1/B1 structure adopts an unexpected conformation representing a closing channel with a trapped L-cis-Diltiazem (Figure 6C–6D and movie S4). In this structure, even with the bound-cGMP, all four subunits adopt the closed conformation similar to the apo state with C-helices down in all subunits (Figure S12). While the pore is trying to close the gate, the presence of the blocker prevents Phe389 from $A1_L$ from rotating back to its original closed position and thereby only three gate-forming phenylalanines retain the closed conformation. The gate closing also squeezes the blocker upward into the tight space between the filter and the gate, causing a steric clash against the filter and resulting in dramatic structural rearrangements in the filter and its vicinity from all subunits (movie S5 and Figure S12). As the closed conformation was not observed in the structures of cGMP-bound CNGA1/B1 in the absence of the blocker, we suspect that the blocker may promote pore closing by drawing the pore-lining inner helices toward a closed conformation. The closed pore may conversely deactivate the CNBD by having the C-helix detached from the ligand-binding pocket as seen in the apo state despite the presence of cGMP, allowing us to capture the channel in a cGMP-bound closed state but with a distorted filter.

Discussion

Here we present a wide spectrum of human CNGA1/B1 structures obtained under various conditions, which, along with electrophysiological analysis, reveals the structural mechanisms underlying some distinct functional properties of native rod CNG. While the CNGA1/B1 heteromer and CNGA1 homomer share a very similar structure in the apo closed state, their structural divergence occurs upon cGMP activation. A central feature of cGMP gating in both CNGA1/B1 and CNGA1 is that the C-helix of the A1 subunit adopts an activated conformation upon cGMP binding and its lever-like upward movement is relayed to the pore-opening motion of S6 at the neighboring subunit through the C-linker

domain. In homomeric CNGA1, all four subunits undergo the same conformation changes that lead to the symmetrical open pore. In cGMP-bound CNGA1/B1, however, the B1 C-helix can either adopt an upward conformation similar to a cGMP-activated A1 subunit or remain downward similar to its apo state despite the presence of cGMP, suggesting a weakened cGMP activation effect on the B1 subunit. Regardless of its C-helix position, B1 subunit in a cGMP-activated CNGA1/B1 structure fails to relay the cGMP-induced conformational changes at the gating apparatus to the pore-opening movement at its S6 as well as the S6 from its right-hand neighbor $A1_R$, yielding an asymmetrical open pore with only two S6 helices adopting an open conformation. This asymmetrical gating mechanism also renders the distinct pharmacological property to the native channel as it generates a perfect space and van der Waals contact environment for L-cis-Diltiazem. While cAMP can also bind in both A1 and B1 subunits similar to cGMP, it does not introduce any conformational changes at the CNBDs and the structure of cAMP-bound CNGA1/B1 remains in the closed state. As the structures of CNBDs in both A1 and B1 subunits are not as well defined as other parts of the channel, we haven't yet been able to identify the structure feature in CNGB1 that conveys higher cAMP sensitivity to native rod CNG, allowing it to be partially activated by cAMP at high concentrations.

STAR METHODS

RESOURCE AVAILABILITY

Lead contact: Further information and requests for resources and reagents should be directed to Youxing Jiang (youxing.jiang@utsouthwestern.edu)

Materials availability: All unique reagents generated in this study are available from the Lead Contact with a completed Materials Transfer Agreement.

Data and code availability:

- The cryo-EM density maps of the human CNGA1/B1 have been deposited in the Electron Microscopy Data Bank under accession numbers EMD-24458 for the high resolution map of the apo state, EMD-24465 for the lower resolution map of the apo state after focused 3D classification, EMD-24461 and EMD-24462 for the cGMP-bound open I and open II, respectively, EMD-24460 for the cAMP-bound, closed state, EMD-24463 for the cGMP-bound, open state with L-cis-Diltiazem, and EMD-24464 for the cGMP-bound, closed state with L-cis-Diltiazem. Atomic coordinates have been deposited in the Protein Data Bank under accession numbers 7RH9 for the apo structure, 7RHL for the apo structure with 3-helix coiled coil, 7RHH and 7RHI for the cGMP-bound open I and open II structures, respectively, 7RHG for the cAMP-bound, closed state, 7RHJ for the open CNGA1/B1 with L-cis-Diltiazem, and 7RHK for the closed CNGA1/B1 with L-cis-Diltiazem.
- This paper does not report original code.
- Any additional information required to reanalyze the data reported in this paper is available from the lead contact upon request.

EXPERIMENTAL MODEL AND SUBJECT DETAILS

Cell Lines—HEK293F cells (Thermo Fisher Scientific) were maintained in FreeStyle 293 Expression Medium (Gibco) at 37°C, 8% CO_2, 130 rpm in a Reach-In CO_2 Incubator (Thermo Fisher Scientific) throughout. HEK293 cells (ATCC) used for electrophysiology were grown in DMEM media (Thermo Fisher Scientific) supplemented with 10% fetal bovine serum (FBS, Thermo Fisher Scientific) and kept in a 37°C, 5% CO_2 incubator.

METHOD DETAILS

Protein expression and purification—A bi-cistronic construct of the human rod CNGA1/B1 channel, with the two genes (CNGA1 and CNGB1) linked by a 22-amino-acid-long P2A self-cleaving peptide, was designed, synthesized, and cloned into the pEZT-BM vector for the expression of heterotetrameric channel proteins. To improve the protein stability and expression level, truncated human CNGA1 (145–690aa, HsCNGA1, NCBI accession: NP_000078.2) and CNGB1 (456–1251aa, HsCNGB1, NCBI accession: NP_001288.3) with Flag tag placed at the N-terminus of both subunits were used in the final bi-cistronic construct (Kim et al., 2020) and expressed in HEK293F cells using the BacMam system (Thermo Fisher Scientific). Bacmids were synthesized using *E. coli* DH10bac cells (Thermo Fisher Scientific) and baculoviruses were produced in Sf9 cells using Cellfectin II reagent (Thermo Fisher Scientific). For protein expression, cultured HEK293F cells were infected with the baculoviruses at a ratio of 1:40 (virus:HEK293F, v/v) and supplemented with 10 mM sodium butyrate to boost protein expression level. Cells were cultured in suspension at 37°C for 48 hr and then harvested by centrifugation at 4,000 g for 15 min. All purification procedures were carried out at 4°C. The cell pellet was re-suspended in buffer A (30 mM HEPES pH 7.4, 300 mM NaCl) supplemented with a protease inhibitor cocktail (2 μg/ml DNase, 0.5 μg/ml pepstatin, 2 μg/ml leupeptin, and 1 μg/ml aprotinin and 0.1 mM PMSF). After homogenization by sonication, HsCNGA1_B1 was extracted with 1% (w/v) Lauryl Maltose Neopentyl Glycol (LMNG, Anatrace) by gentle agitation for 2 hr. After extraction, the supernatant was collected by centrifugation at 40,000 g for 30 min and incubated with anti-Flag M2 affinity resin (Genescript) by gentle agitation for 1 hr. The resin was then collected on a disposable gravity column (Bio-Rad) and washed with 20-column volume of Buffer A supplemented with 0.03% (w/v) LMNG and followed by 20-column volume of Buffer A supplemented with 0.06% Digitonin (w/v). HsCNGA1/B1 was eluted in Buffer A with 0.06% (w/v) Digitonin and 0.2 mg/ml Flag peptide. The protein eluate was concentrated and further purified by size-exclusion chromatography on a Superose 6 10/300 GL column (GE Healthcare) in Buffer A with 0.06% (w/v) Digitonin. The peak fractions were collected and concentrated to about 6.5 mg/ml for cryo-EM analysis. To prepare the protein samples in complex with ligands and blocker, 10 mM cAMP, 1 mM cGMP, or 1mM L-cis-Diltiazem was added to the protein samples about 2 hours before they were applied to the grids and plunge frozen.

The HsCNGA1/B1(G848E), HsCNGA1/B1(R880G), and HsCNGA1ΔCLZ/B1 (deletion of C-terminal residues 619–690 in A1) mutant constructs for electrophysiological recordings were generated using QuikChange (Agilent).

HEK293 (CRL-1573) cell lines were purchased from and authenticated by the American Type Culture Collection (ATCC, Manassas, VA). HEK293F cells (RRID: CVCL_D603) were purchased from and authenticated by Thermo Fisher Scientific. The cell lines were tested negative for mycoplasma contamination.

Cryo-EM sample preparation and data acquisition—Purified HsCNGA1/B1 samples in various conditions at 6.5 mg/ml were applied to a glow-discharged Quantifoil R1.2/1.3 300-mesh gold holey carbon grid (Quantifoil, Micro Tools GmbH, Germany), blotted for 4.0 s under 100% humidity at 4°C and plunged into liquid ethane using a Mark IV Vitrobot (FEI).

For the data of HsCNGA1/B1 samples in the cGMP-bound state, movies were acquired on a Titan Krios microscope (FEI) operated at 300 kV with a K3 Summit direct electron detector (Gatan), using a slit width of 20 eV on a GIF-Quantum energy filter. Images were recorded with Serial EM in super-resolution counting mode with a calibrated super resolution pixel size of 0.4085 Å. The defocus range was set from −0.9 to −2.2 μm. Each movie was dose-fractionated to 50 frames under a dose rate of 1 e^{-}/pixel/frame, resulting in a total dose of about 50 $e^{-}/Å^{2}$.

The data of HsCNGA1/B1 samples in apo, cAMP-bound, and L-cis-Diltiazem-bound states were collected at the Janelia cryo-EM facility. Movies were acquired similarly to the samples in the cGMP-bound state. The Krios microscope was equipped with a Cs corrector. Each movie was dose-fractionated to 60 frames with a dose rate of $1e^{-}$/Å2/frame for a total dose of $60e^{-}$/Å2. The calibrated super resolution pixel sizes for HsCNGA1/B1 in apo, cAMP-bound, and L-cis-Diltiazem-bound states were 0.421 Å, 0.4205 Å, and 0.4195 Å, respectively. All data were collected using the CDS (Correlated Double Sampling) mode of the K3 camera with electron dose rates between 7 and 10 e^{-}/pixel/s.

Image processing—Cryo-EM data were processed following the subsequent general scheme, with modifications to different datasets (see below). First, movie frames were motion corrected and binned two times and dose-weighted using MotionCor2 (Zheng et al., 2017). The CTF parameters of the micrographs were estimated using the GCTF program (Zhang, 2016). The rest of the image processing steps was carried out using RELION 3.1 (Scheres, 2012; Zivanov et al., 2018). After CTF estimation, micrographs were manually inspected to remove images with bad defocus values, ice contamination, or carbon. Particles were selected using Gautomatch (Kai Zhang, http://www.mrc-lmb.cam.ac.uk/kzhang/) and extracted using a binning factor of 3. Next, particles were subjected to one round of 2D classification in Relion, followed by one round of 3D classification with alignment on selected particles from the 2D classification job. The structure of the homo-tetrameric CNGA1 channel (EMD-23306) (Xue et al., 2021) was low-pass filtered to 30Å and used as the initial reference. Classes that showed clear features of the CNG channel were combined and subjected to 3D auto-refinement and another round of 3D classification without performing particle alignment using a soft mask around the protein portion of the density. The best resolving class was then re-extracted with the original pixel size and further refined. Beam tilt, anisotropic magnification, and per-particle CTF estimations were performed in Relion 3.1 to improve the resolution of the final reconstruction. 3D

classification and refinement steps were performed using C1 symmetry, unless otherwise noted. All resolution was reported according to the gold-standard Fourier shell correlation (FSC) using the 0.143 criterion (Henderson et al., 2012). Local resolution was estimated using Relion.

For the dataset of apo HsCNGA1/B1, a total of 8,042 movies were collected and 7,619 were selected after motion correction and CTF estimation. A total number of 1,827,066 particles were extracted from the selected micrographs and were subjected to one round of 2D classification, from which 1,356,350 particles were selected. After the initial 3D classification, 1,111,618 particles were selected and subjected to a 3D auto-refinement job. As is shown in Figure S3B, particles of the apo HsCNGA1/B1 adopt different orientations in different classes. Therefore, we imposed C4 symmetry in this refinement step to force the particles to adopt the same orientation and to align them along the pseudo-symmetric axis. This also simplifies the procedure of manual rotation of the particles (see below). Next, a soft mask excluding the micelle density was applied and particles were sorted into 6 classes without performing the alignment. This step was performed without imposing any symmetry, allowing the separation of particles with subunit CNGB1 at various positions into 5 of the 6 total classes (Figure S3B), which were then manually rotated to the consensus orientation in that of class 1. From this classification, 789,741 particles were selected and further refined. To better resolve the helix bundle and subunit CNGB1, two separate classification procedures were performed. First, a soft mask around subunit CNGB1 was used in a focused classification run without particle alignment. 687,702 particles were selected from this classification and refine to an overall resolution of 2.61Å. Second, a soft mask around the helix bundle was applied after a focused refinement of the remaining density. Then a 3D classification without particle alignment was performed and 53,732 particles (with best-resolved helix bundle features) were selected and refined to an overall resolution of 3.03Å (Figure S3).

For the dataset of cGMP-bound HsCNGA1/B1, a total of 5,487 movies were collected and 4,877 were selected after motion correction and CTF estimation. A total number of 884,714 particles were extracted from the selected micrographs and were subjected to one round of 2D classification, from which 455,123 particles were selected. After the initial 3D classification, 297,358 particles were selected and subjected to a 3D auto-refinement job. Next, a soft mask excluding the micelle density was applied and particles were sorted into 5 classes without performing the alignment. From this, two conformations (each with 54,022 and 209,597 particles) of the channel were selected and further refined, yielding two maps both at 3.31Å overall resolution (Figure S4).

For the dataset of cAMP-bound HsCNGA1/B1, a total of 5,600 movies were collected and 5,136 were selected after motion correction and CTF estimation. A total number of 1,012,458 particles were extracted from the selected micrographs and were subjected to one round of 2D classification, from which 872,048 particles were selected. After the initial 3D classification, 632,060 particles were selected and subjected to a 3D auto-refinement job. Next, a soft mask excluding the micelle density was applied and particles were sorted into 5 classes without performing the alignment. This resulted in classes of particles with subunit CNGB1 at various positions. To better resolve the structure, especially the subunit CNGB1,

the particles were manually rotated to the consensus orientation, followed by another round of classification with no particle alignment. This time, a soft mask around subunit CNGB1 was applied. From this classification, 326,371 particles were selected and further refined, yielding a map at an overall resolution of 2.88Å (Figure S5).

For the dataset of L-cis-Diltiazem-bound HsCNGA1/B1, a total of 9,408 movies were collected and 8,752 were selected after motion correction and CTF estimation. A total number of 1,923,317 particles were extracted from the selected micrographs and were subjected to one round of 2D classification, from which 1,526,674 particles were selected. After the initial 3D classification, 878,654 particles were selected and subjected to a 3D auto-refinement job. In this refinement job, the sampling parameters in Relion were changed to 15 degrees for initial angular sampling, 10 pixels for initial offset range, and 2 pixels for the initial offset step. Next, a soft mask excluding the micelle density was applied and particles were sorted into 5 classes without performing the alignment. From this, two classes (each with 187,429 and 105,005 particles) were selected and further refined, yielding two maps at 2.88Å and 3.27Å overall resolution, respectively (Figure S6).

Model building, refinement, and validation—All EM maps of HsCNGA1/B1 in the open and closed states show high quality density for de novo model building in Coot (Emsley et al., 2010), facilitated by the previous cryo-EM structure of HsCNGA1 (PDB:7LFT; PDB:7LFW). Models were manually adjusted in Coot and refined against summed maps using the phenix.real_space_refine, with secondary structure restraints applied (Adams et al., 2010). The model was validated using previously described methods to avoid overfitting (Amunts et al., 2014; DiMaio et al., 2013). The final structural models contain residues 156–605 from the CNGA1 subunit and residues 645–748 and 757–1084 from the CNGB1 subunit. The N-terminal residues 145–155 and the C-terminal residues 606–690 of CNGA1 were disordered in the structure. The N-terminal residues 456–644 and the C-terminal residues 1085–1251 of CNGB1 were disordered in the structure. The binding of the cGMP ligand appears to make the CNBD region more dynamic, resulting in a less well-resolved EM density map at CNBD in the cGMP-bound structure as compared to that in the apo structure. Therefore, CNBDs from the apo HsCNGA1/B1 and the cGMP-bound HsCNGA1 homomer structures were used to facilitate the model building for the CNBD part of the cGMP-bound HsCNGA1/B1 structure. The regions that did not fit the density map were adjusted manually in Coot. The statistics of the geometries of the models were generated using MolProbity (Chen et al., 2010). All the figures were prepared in PyMol (Schrödinger, LLC.) and UCSF Chimera (Pettersen et al., 2004). Pore radii were calculated using the HOLE program (Smart et al., 1996). Only poly-A helices corresponding to CLZ of A1 and D-helix of B1were modeled to the C-terminal region of apo HsCNGA1/B1 using the lower resolution map after focused 3D classification.

Electrophysiology—1.5 μg of the pEZT-BM vector containing HsCNGA1/B1 or its mutant was transfected into HEK293 cells using Lipofectamine 2000 (Life Technology). To facilitate cell selection for patch clamp, 0.2 μg of the pNGFP-EU vector containing GFP was co-transfected into HEK293 cells (Kawate and Gouaux, 2006). 48 hours after transfection, cells were dissociated by trypsin treatment and kept in a complete serum-containing medium

and re-plate on 35 mm tissue culture dishes in a tissue culture incubator until recording. Channel currents were recorded using whole-cell inside-out and outside-out configurations. For the electrophysiology of the HsCNGA1 homomer, the pEZT-BM vector containing the full-length HsCNGA1 was used in the transfection. The full-length HsCNGA1 exhibits similar Ca^{2+} blockage and cGMP activation properties to the N-terminal truncation mutant (Xue et al., 2021), but elicits larger currents than the truncation construct.

Patch pipettes were pulled from borosilicate glass (Harvard Apparatus) and heat-polished to a resistance of 3–5 MΩ. After the patch pipette was attached to the cell membrane, a giga-seal (> 10GΩ) was formed by gentle suction. The whole-cell configuration was formed by a short zap or suction to rupture the patch. The outside-out configuration was formed by pulling the pipette away from the cell after the whole cell configuration was formed. The inside-out configuration was formed by pulling the pipette away from the cell, and the pipette tip was exposed to the air for a short period in some cases. Data were acquired using an AxoPatch 200B amplifier (Molecular Devices) with a low-pass analog filter set to 1 kHz. The current signal was sampled at a rate of 20 kHz using a Digidata 1550B digitizer (Molecular Devices) and further analyzed with pClamp11 software (Molecular Devices).

The cGMP and cAMP activation of HsCNGA1/B1 or HsCNGA1 were recorded in excised patches (inside-out patches). The pipette solution contained 140 mM NaCl, 4 mM KCl, 1 mM EGTA, and 10 mM HEPES, pH 7.4, whereas the bath solution contained 140 mM KCl, 5 mM EGTA, and 10 mM HEPES, pH 7.4. Various concentrations of cGMP or cAMP were added to the bath solution. The extracellular Ca^{2+} blockage and L-cis-diltiazem inhibition of HsCNGA1/B1 were recorded using patch clamp in whole-cell configuration. The pipette solution contained 140 mM KCl, 5 mM EGTA, 10 mM HEPES, pH 7.4, and 1 mM cGMP. The bath solution contained 140 mM NaCl, 4 mM KCl, 1 mM EGTA, and 10 mM HEPES, pH 7.4. Free calcium concentrations in the bath solution were controlled by mixing 1 mM EGTA with appropriate amounts of $CaCl_2$ calculated using MAXCHELATOR (https://somapp.ucdmc.ucdavis.edu/pharmacology/bers/maxchelator/). Various concentrations of L-cis-Diltiazem were added to the bath solution. The outside-out configuration was used to record the single channel currents of HsCNGA1/B1 and HsCNGA1/B1(R880G) mutant, and the pipette solution and bath solution were the same as whole-cell configuration with 50 μM cGMP in the pipette. To generate the current and voltage relationship, the membrane potential was held at 0 mV, followed by voltage pulses ramp from −100 to +100 mV over 800 ms duration.

QUANTIFICATION AND STATISTICAL ANALYSIS

Data analysis was performed using OriginPro 8 (OriginLab). Statistical details are described in the Results and Figure Legends. All data are mean ± SEM. Exact values of n are reported where appropriate. Depending on the experiment, n represents number of independent measurements.

Supplementary Material

Refer to Web version on PubMed Central for supplementary material.

Acknowledgments:

Single particle cryo-EM data were collected at the University of Texas Southwestern Medical Center Cryo-EM Facility that is funded by the CPRIT Core Facility Support Award RP170644 and the Howard Hughes Medical Institute Janelia Cryo-EM Facility. We thank Rui Yan at the Janelia Cryo-EM Facility for help in microscope operation and data collection. This work was supported in part by the Howard Hughes Medical Institute (to Y.J.) and by grants from the National Institute of Health (R35GM140892 to Y.J.), and the Welch Foundation (Grant I-1578 to Y.J.).

References

Adams PD, Afonine PV, Bunkoczi G, Chen VB, Davis IW, Echols N, Headd JJ, Hung LW, Kapral GJ, Grosse-Kunstleve RW, et al. (2010). PHENIX: a comprehensive Python-based system for macromolecular structure solution. Acta Crystallogr D Biol Crystallogr 66, 213–221. [PubMed: 20124702]

Amunts A, Brown A, Bai XC, Llacer JL, Hussain T, Emsley P, Long F, Murshudov G, Scheres SHW, and Ramakrishnan V (2014). Structure of the yeast mitochondrial large ribosomal subunit. Science 343, 1485–1489. [PubMed: 24675956]

Biel M, Zong X, Ludwig A, Sautter A, and Hofmann F (1999). Structure and function of cyclic nucleotide-gated channels. Rev Physiol Biochem Pharmacol 135, 151–171. [PubMed: 9932483]

Bonigk W, Altenhofen W, Muller F, Dose A, Illing M, Molday RS, and Kaupp UB (1993). Rod and cone photoreceptor cells express distinct genes for cGMP-gated channels. Neuron 10, 865–877. [PubMed: 7684234]

Bonigk W, Bradley J, Muller F, Sesti F, B. I, Ronnett GV, Kaupp UB, and Frings S (1999). The native rat olfactory cyclic nucleotide-gated channel is composed of three distinct subunits. J Neurosci 19, 5332–5347. [PubMed: 10377344]

Bradley J, Li J, Davidson N, Lester HA, and Zinn K (1994). Heteromeric Olfactory Cyclic Nucleotide-Gated Channels - a Subunit That Confers Increased Sensitivity to Camp. P Natl Acad Sci USA 91, 8890–8894.

Bradley J, Reisert J, and Frings S (2005). Regulation of cyclic nucleotide-gated channels. Curr Opin Neurobiol 15, 343–349. [PubMed: 15922582]

Chen TY, Illing M, Molday LL, Hsu YT, Yau KW, and Molday RS (1994). Subunit 2 (or Beta) of Retinal Rod Cgmp-Gated Cation Channel Is a Component of the 240-Kda Channel-Associated Protein and Mediates Ca2+-Calmodulin Modulation. P Natl Acad Sci USA 91, 11757–11761.

Chen TY, Peng YW, Dhallan RS, Ahamed B, Reed RR, and Yau KW (1993). A new subunit of the cyclic nucleotide-gated cation channel in retinal rods. Nature 362, 764–767. [PubMed: 7682292]

Chen VB, Arendall WB 3rd, Headd JJ, Keedy DA, Immormino RM, Kapral GJ, Murray LW, Richardson JS, and Richardson DC (2010). MolProbity: all-atom structure validation for macromolecular crystallography. Acta Crystallogr D Biol Crystallogr 66, 12–21. [PubMed: 20057044]

Craven KB, and Zagotta WN (2006). CNG and HCN channels: two peas, one pod. Annu Rev Physiol 68, 375–401. [PubMed: 16460277]

Dhallan RS, Yau KW, Schrader KA, and Reed RR (1990). Primary structure and functional expression of a cyclic nucleotide-activated channel from olfactory neurons. Nature 347, 184–187. [PubMed: 1697649]

DiMaio F, Zhang JJ, Chiu W, and Baker D (2013). Cryo-EM model validation using independent map reconstructions. Protein Science 22, 865–868. [PubMed: 23592445]

Emsley P, Lohkamp B, Scott WG, and Cowtan K (2010). Features and development of Coot. Acta Crystallogr D Biol Crystallogr 66, 486–501. [PubMed: 20383002]

Finn JT, Grunwald ME, and Yau KW (1996). Cyclic nucleotide-gated ion channels: An extended family with diverse functions. Annual Review of Physiology 58, 395–426.

Gerstner A, Zong X, Hofmann F, and Biel M (2000). Molecular cloning and functional characterization of a new modulatory cyclic nucleotide-gated channel subunit from mouse retina. J Neurosci 20, 1324–1332. [PubMed: 10662822]

Haynes LW (1992). Block of the cyclic GMP-gated channel of vertebrate rod and cone photoreceptors by l-cis-diltiazem. J Gen Physiol 100, 783–801. [PubMed: 1282145]

Henderson R, Sali A, Baker ML, Carragher B, Devkota B, Downing KH, Egelman EH, Feng Z, Frank J, Grigorieff N, et al. (2012). Outcome of the first electron microscopy validation task force meeting. Structure 20, 205–214. [PubMed: 22325770]

Hsu YT, and Molday RS (1993). Modulation of the Cgmp-Gated Channel of Rod Photoreceptor Cells by Calmodulin (Vol 361, Pg 76, 1993). Nature 365, 279–279.

Kaupp UB (1995). Family of Cyclic-Nucleotide Gated Ion Channels. Current Opinion in Neurobiology 5, 434–442. [PubMed: 7488843]

Kaupp UB, Niidome T, Tanabe T, Terada S, Bonigk W, Stuhmer W, Cook NJ, Kangawa K, Matsuo H, Hirose T, et al. (1989). Primary structure and functional expression from complementary DNA of the rod photoreceptor cyclic GMP-gated channel. Nature 342, 762–766. [PubMed: 2481236]

Kaupp UB, and Seifert R (2002). Cyclic nucleotide-gated ion channels. Physiol Rev 82, 769–824. [PubMed: 12087135]

Kawate T, and Gouaux E (2006). Fluorescence-detection size-exclusion chromatography for precrystallization screening of integral membrane proteins. Structure 14, 673–681. [PubMed: 16615909]

Kim JJ, Gharpure A, Teng JF, Zhuang YX, Howard RJ, Zhu ST, Noviello CM, Walsh RM, Lindahl E, and Hibbs RE (2020). Shared structural mechanisms of general anaesthetics and benzodiazepines. Nature 585, 303–+. [PubMed: 32879488]

Kizhatil K, Baker SA, Arshavsky VY, and Bennett V (2009). Ankyrin-G Promotes Cyclic Nucleotide-Gated Channel Transport to Rod Photoreceptor Sensory Cilia. Science 323, 1614–1617. [PubMed: 19299621]

Korschen HG, Illing M, Seifert R, Sesti F, Williams A, Gotzes S, Colville C, Muller F, Dose A, Godde M, et al. (1995). A 240 kDa protein represents the complete beta subunit of the cyclic nucleotide-gated channel from rod photoreceptor. Neuron 15, 627–636. [PubMed: 7546742]

Li M, Zhou X, Wang S, Michailidis I, Gong Y, Su D, Li H, Li X, and Yang J (2017). Structure of a eukaryotic cyclic-nucleotide-gated channel. Nature 542, 60–65. [PubMed: 28099415]

Liu ZQ, Chen O, Wall JBJ, Zheng M, Zhou Y, Wang L, Vaseghi HR, Qian L, and Liu JD (2017). Systematic comparison of 2A peptides for cloning multi-genes in a polycistronic vector. Sci Rep-Uk 7.

Matulef K, and Zagotta WN (2003). Cyclic nucleotide-gated ion channels. Annu Rev Cell Dev Biol 19, 23–44. [PubMed: 14570562]

Michalakis S, Zong XG, Becirovic E, Hammelmann V, Wein T, Wanner KT, and Biel M (2011). The Glutamic Acid-Rich Protein Is a Gating Inhibitor of Cyclic Nucleotide-Gated Channels. J Neurosci 31, 133–141. [PubMed: 21209198]

Peng C, Rich ED, and Varnum MD (2004). Subunit configuration of heteromeric cone cyclic nucleotide-gated channels. Neuron 42, 401–410. [PubMed: 15134637]

Pettersen EF, Goddard TD, Huang CC, Couch GS, Greenblatt DM, Meng EC, and Ferrin TE (2004). UCSF Chimera--a visualization system for exploratory research and analysis. J Comput Chem 25, 1605–1612. [PubMed: 15264254]

Poetsch A, Molday LL, and Molday RS (2001). The cGMP-gated channel and related glutamic acid-rich proteins interact with peripherin-2 at the rim region of rod photoreceptor disc membranes. Journal of Biological Chemistry 276, 48009–48016.

Scheres SH (2012). RELION: implementation of a Bayesian approach to cryo-EM structure determination. J Struct Biol 180, 519–530. [PubMed: 23000701]

Shammat IM, and Gordon SE (1999). Stoichiometry and arrangement of subunits in rod cyclic nucleotide-gated channels. Neuron 23, 809–819. [PubMed: 10482246]

Shuart NG, Haitin Y, Camp SS, Black KD, and Zagotta WN (2011). Molecular mechanism for 3:1 subunit stoichiometry of rod cyclic nucleotide-gated ion channels. Nat Commun 2.

Smart OS, Neduvelil JG, Wang X, Wallace BA, and Sansom MS (1996). HOLE: a program for the analysis of the pore dimensions of ion channel structural models. J Mol Graph 14, 354–360, 376. [PubMed: 9195488]

Trudeau MC, and Zagotta WN (2003). Calcium/calmodulin modulation of olfactory and rod cyclic nucleotide-gated ion channels. J Biol Chem 278, 18705–18708. [PubMed: 12626507]

Weitz D, Ficek N, Kremmer E, Bauer PJ, and Kaupp UB (2002). Subunit stoichiometry of the CNG channel of rod photoreceptors. Neuron 36, 881–889. [PubMed: 12467591]

Xue J, Han Y, Zeng W, Wang Y, and Jiang Y (2021). Structural mechanisms of gating and selectivity of human rod CNGA1 channel. Neuron 109, 1302–1313 e1304. [PubMed: 33651975]

Yau KW, and Baylor DA (1989). Cyclic GMP-activated conductance of retinal photoreceptor cells. Annu Rev Neurosci 12, 289–327. [PubMed: 2467600]

Zagotta WN, Olivier NB, Black KD, Young EC, Olson R, and Gouaux E (2003). Structural basis for modulation and agonist specificity of HCN pacemaker channels. Nature 425, 200–205. [PubMed: 12968185]

Zagotta WN, and Siegelbaum SA (1996). Structure and function of cyclic nucleotide-gated channels. Annu Rev Neurosci 19, 235–263. [PubMed: 8833443]

Zhang K (2016). Gctf: Real-time CTF determination and correction. J Struct Biol 193, 1–12. [PubMed: 26592709]

Zheng J, Trudeau MC, and Zagotta WN (2002). Rod cyclic nucleotide-gated channels have a stoichiometry of three CNGA1 subunits and one CNG131 subunit. Neuron 36, 891–896. [PubMed: 12467592]

Zheng J, and Zagotta WN (2004). Stoichiometry and assembly of olfactory cyclic nucleotide-gated channels. Neuron 42, 411–421. [PubMed: 15134638]

Zheng SQ, Palovcak E, Armache JP, Verba KA, Cheng Y, and Agard DA (2017). MotionCor2: anisotropic correction of beam-induced motion for improved cryo-electron microscopy. Nat Methods 14, 331–332. [PubMed: 28250466]

Zheng X, Fu Z, Su D, Zhang Y, Li M, Pan Y, Li H, Li S, Grassucci RA, Ren Z, et al. (2020). Mechanism of ligand activation of a eukaryotic cyclic nucleotide-gated channel. Nat Struct Mol Biol 27, 625–634. [PubMed: 32483338]

Zhong H, Molday LL, Molday RS, and Yau KW (2002). The heteromeric cyclic nucleotide-gated channel adopts a 3A:1B stoichiometry. Nature 420, 193–198. [PubMed: 12432397]

Zivanov J, Nakane T, Forsberg BO, Kimanius D, Hagen WJ, Lindahl E, and Scheres SH (2018). New tools for automated high-resolution cryo-EM structure determination in RELION-3. Elife 7.

Highlights:

- Determine the structures of the native rod CNG channel in various states.
- Reveal the structural basis of 3:1 subunit stoichiometry of CNGA1/B1 heterotetramer.
- Reveal the asymmetrical gating of the native rod CNG channel upon cGMP activation.
- Provide structural insight into the L-cis-Diltiazem blocking of the native CNG.

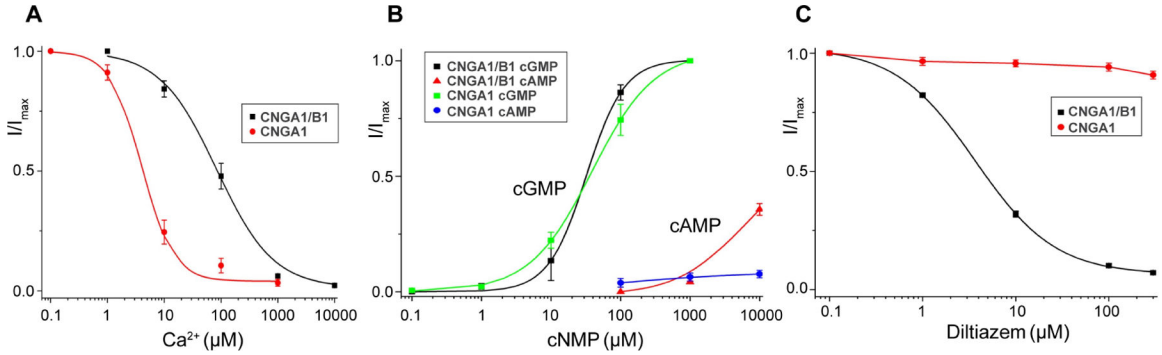

Figure 1. Functional characterization of human CNGA1and CNGA1/B1.

See also Figure S1–S2

(A) Ca^{2+} inhibition of CNGA1 and CNGA1/B1 measured at −100 mV using patch clamp in whole-cell configuration. Curves are least square fits to the Hill equation with K_i=4.02±1.03 μM, n=1.56±0.36 for CNGA1, and K_i=83.8±9.8 μM, n=0.87±0.15 for CNGA1/B1. Data points are mean ± SEM (n=5 independent experiments).

(B) cGMP and cAMP activation of CNGA1 and CNGA1/B1 measured at 100 mV using patch clamp in inside-out configuration. Curves for cGMP activation are least square fits to the Hill equation with EC_{50}=39.4±5.8 μM, n=0.90±0.11 for CNGA1; EC_{50}=32.2±2.1 μM, n=1.59±0.10 for CNGA1/B1. Data points are mean ± SEM (n=5 independent experiments).

(C) L-cis-Diltiazem blocking of CNGA1 and CNGA1/B1 measured at 100 mV using patch clamp in whole-cell configuration. Curve for block in CNGA1/B1 is least square fit to the Hill equation with K_i=3.68±0.13 μM, n=1.01±0.03. Data points are mean ± SEM (n=5 independent experiments).

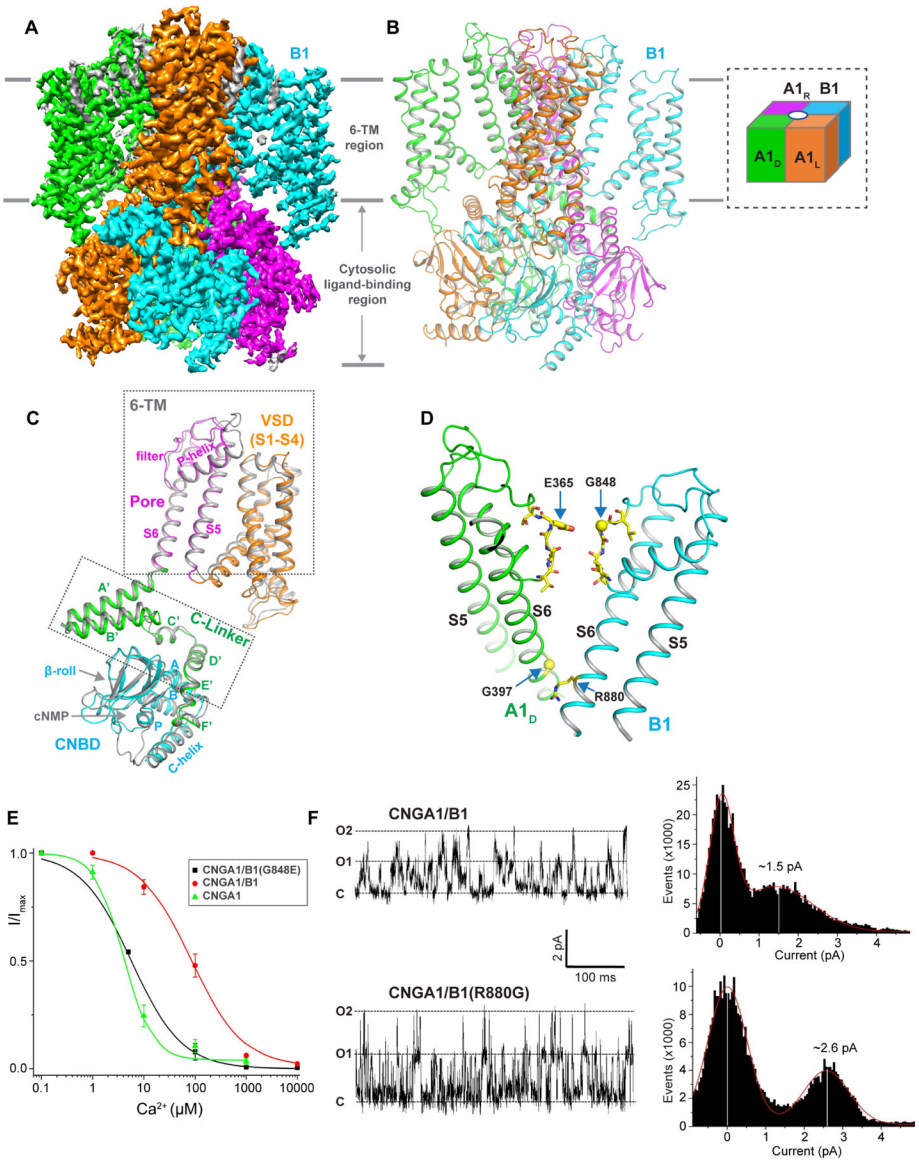

Figure 2. Overall structure of human CNGA1/B1.

See also Figure S3–S9 and Table S1

(A) Side view of 3-D reconstruction of apo CNGA1/B1 with each subunit individually colored. Lipid density is shown in grey.

(B) Side view of cartoon representation of the apo CNGA1/B1 structure with subunits arrangement shown in inset.

(C) Structural comparison between the apo B1 subunit with each domain individually colored and the apo A1 subunit (grey).

(D) Structural differences between A1 and B1 subunits along the ion conduction pathway.

(E) Ca^{2+} inhibition of CNGA1/B1(G848E) measured at −100 mV using patch clamp in whole-cell configuration. Curve is least square fit to the Hill equation with K_i=5.70±0.16 μM, n=0.88±0.03. Data of Ca^{2+} inhibition of CNGA1 and CNGA1/B1 from Figure 1A are also shown for comparison. Data points are mean ± SEM (n=5 independent experiments).

(F) Single channel traces recorded at 100 mV in outside-out configuration and the current amplitude histograms of CNGA1/B1 and CNGA1/B1(R880G) mutant. The pipette solution contains 50 μM cGMP.

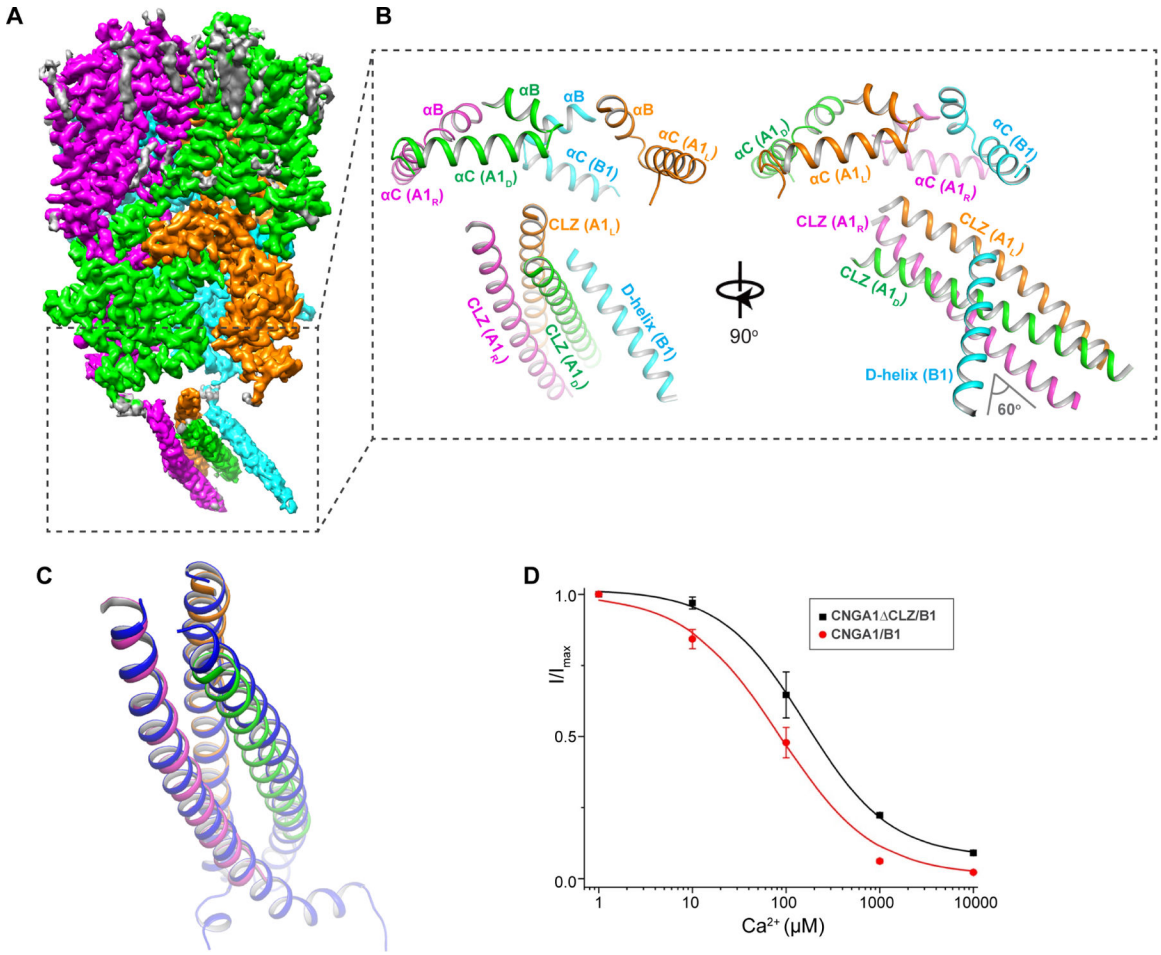

Figure 3. C-terminal CLZ region of CNGA1/B1.

See also Figure S3 and S10

(A) Side view of EM map after focused 3-D reconstruction of apo CNGA1/B1 with mask around the C-terminal region (boxed region).

(B) Cartoon representation of the apo CNGA1/B1 structure at the C-terminal region formed by CLZ domains from A1 subunits and D-helix from B1 subunit.

(C) Structural comparison of CLZ-formed 3-helix coiled coil from this study and the crystal structure (blue, PDB code: 3SWF).

(D) Ca^{2+} inhibition of CNGA1ΔCLZ/B1 mutant measured at −100 mV using patch clamp in whole-cell configuration. Curve is least square fit to the Hill equation with K_i=161±19.5 μM, n=0.96±0.11. Data of Ca^{2+} inhibition of CNGA1/B1 from Figure 1A are also shown for comparison. Data points are mean ± SEM (n=5 independent experiments).

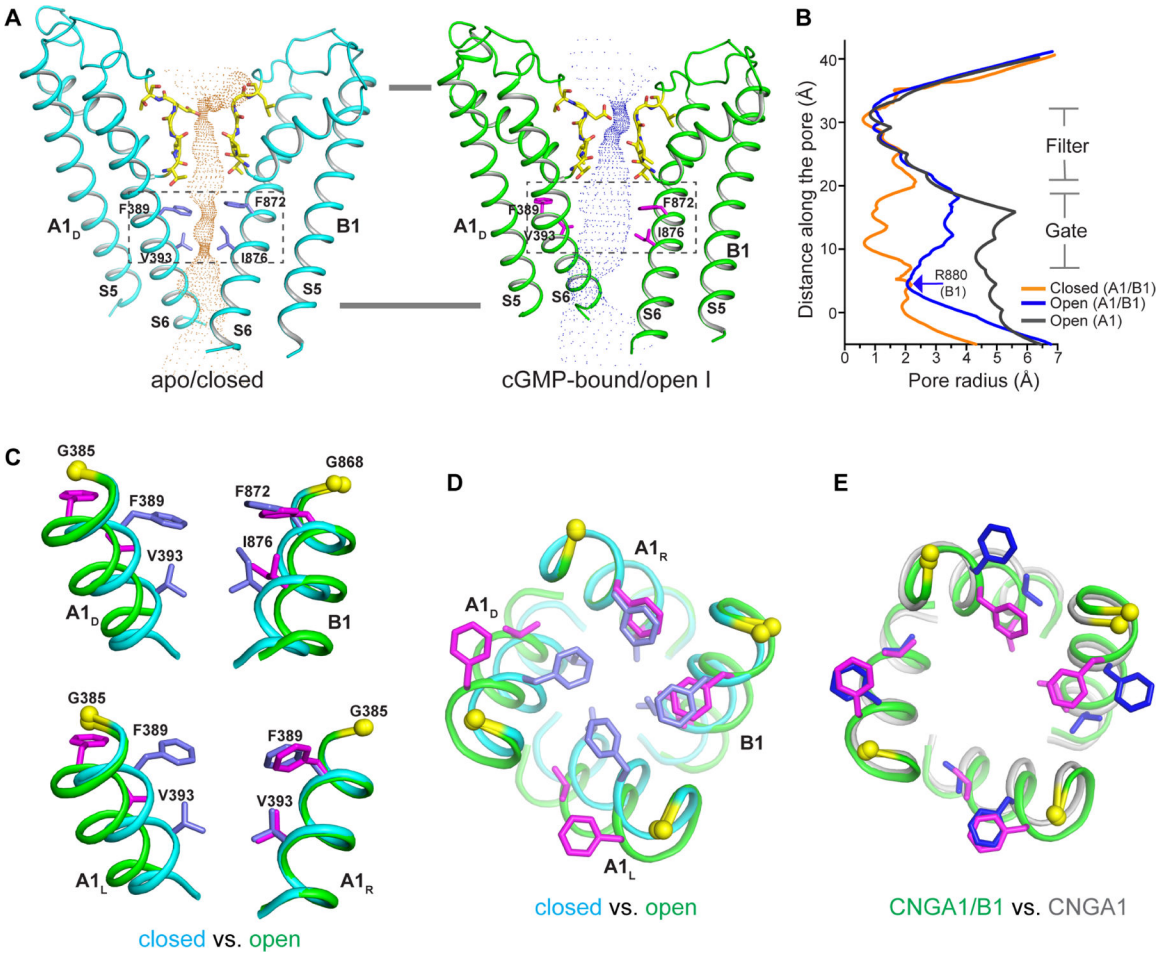

Figure 4. Asymmetrical opening of CNGA1/B1 pore.

(A) The ion conduction pore of the apo closed (left) and cGMP-bound open (right) CNGA1/B1 with only $A1_D$ and B1 subunits shown for clarity. Central ion pathway is marked with dotted mesh. Key gating and filter residues are shown as sticks.

(B) Pore radius along the central axis in the open (in blue) and closed (in orange) states of CNGA1/B1 as well as in the open CNGA1 homomer (in grey).

(C) Structural comparison of the central gate of CNGA1/B1 (boxed region in **A**) between the open (green, with gating residues in magenta) and closed (cyan, with gating residues in blue) states in side view. Only the S6 helices and gating residues from two diagonal subunits are shown in the superposition. Yellow spheres mark the Cα atoms of glycine gating hinges (G385 in A1 and G868 in B1).

(D) Structural comparison of the central gate between the closed (cyan) and open (green) states viewed from extracellular side.

(E) Structural comparison of the open central gate between CNGA1/B1 and CNGA1 (grey, with gating residues in blue) viewed from extracellular side.

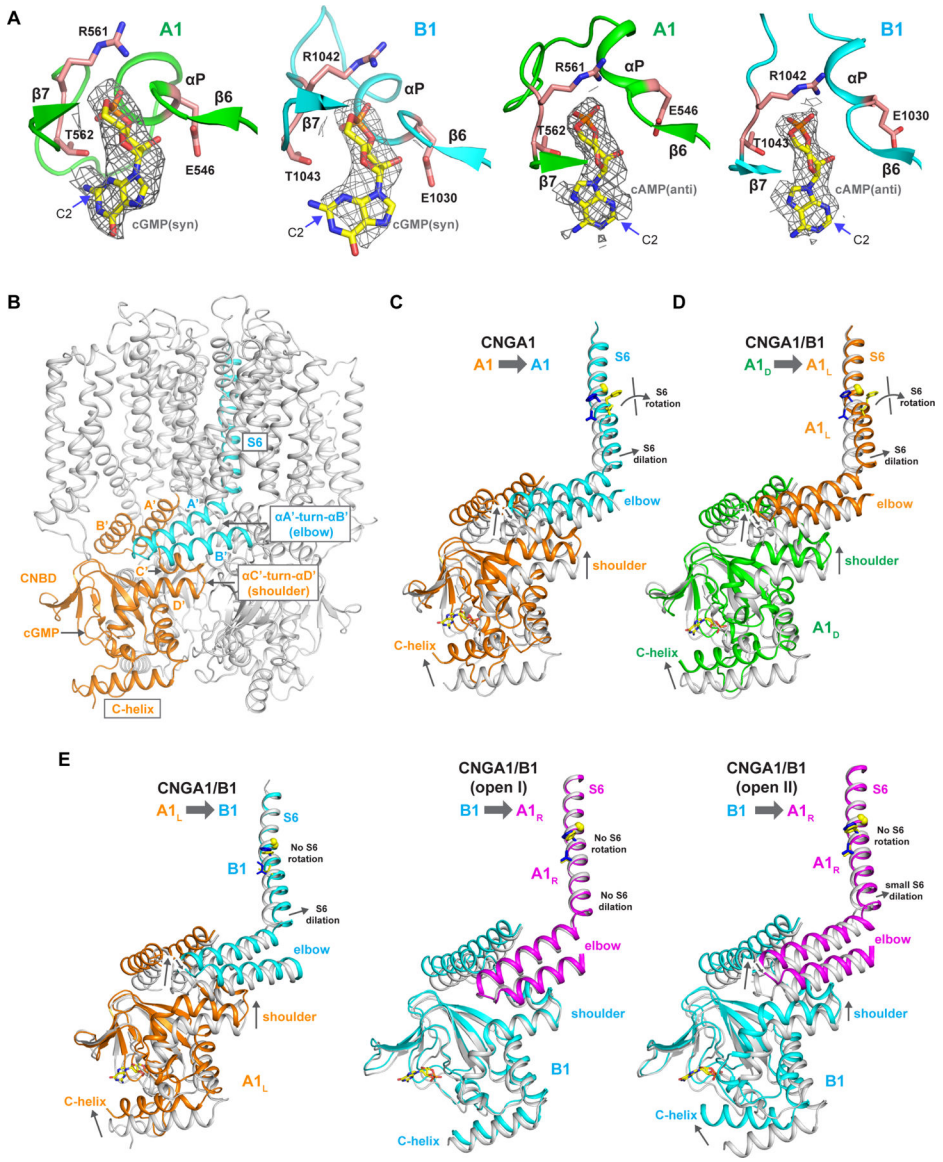

Figure 5. cNMP binding and cGMP activation of CNGA1/B1.

See also Figure S11

(A) Zoomed-in views of cGMP and cAMP binding in A1 and B1 subunits. The density maps for cGMP (in syn conformation) and cAMP (in anti conformation) are contoured at 5 σ and 4 σ, respectively. Key ligand interacting residues are shown in stick.

(**B)** Structure of apo CNGA1 with the key regions important for the relay of global gating conformational changes between two neighboring subunits highlighted. CNBD from one subunit is colored in orange and helix A'-turn-helix B' and S6 from the neighboring subunit in cyan.

(C) Structural comparison between the closed (grey) and open CNGA1 (colored) at the region highlighted in (B). Arrows indicate the cGMP-induced movements relayed from C-helix of one subunit (orange) to the S6 of the neighboring subunit (cyan) from closed to open state at various parts of cytosolic region.

(D) Structural comparison between the closed (grey) and open CNGA1/B1 (colored) illustrating the relay of gating conformational changes from $A1_D$ (green) to $A1_L$ (orange) subunit. The conformational relay between $A1_R$ and $A1_D$ is similar.
(E) The relays of gating conformational changes from $A1_L$ (orange) to B1 (cyan) subunit (left), from B1 (cyan) to $A1_R$ (magenta) subunit in open I state (middle), and from B1 (cyan) to $A1_R$ (magenta) subunit in open II state (right).

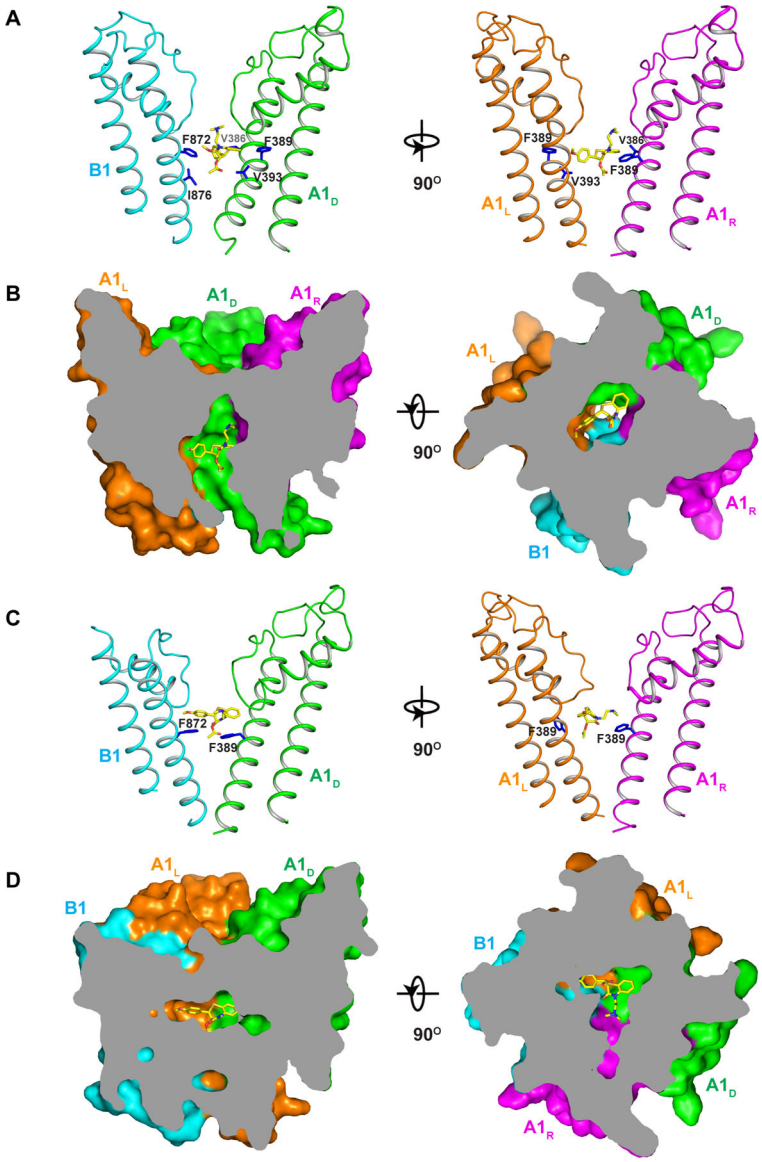

Figure 6. L-cis-Diltiazem blocking of CNGA1/B1.

See also Figure S12

(A) Side views of L-cis-Diltiazem blocking at the gate of an open CNGA1/B1 pore with two diagonal subunits shown for clarity. Key residues in close contact with the blocker are shown as blue sticks.

(B) Side (left) and top (right) views of the cross sections of the surface-rendered open pore with L-cis-Diltiazem blocking at the center.

(C) Side views of trapped L-cis-Diltiazem above the gate of a closed CNGA1/B1 pore with only two diagonal subunits shown for clarity. Only side chains of F389 of A1 and F872 of B1 are shown (blue sticks).

(D) Side (left) and top (right) views of the cross sections of the surface-rendered closed pore with L-cis-Diltiazem trapped below the filter.

KEY RESOURCES TABLE

REAGENT or RESOURCE	SOURCE	IDENTIFIER
Bacterial and Virus Strains		
DH125α	Thermo Fisher Scientific	Cat# C404003
DH10Bac	Thermo Fisher Scientific	Cat# 10361012
Chemicals, Peptides, and Recombinant Proteins		
Sodium Butyrate	Sigma-Aldrich	Cat# 303410
Lauryl Maltose Neopentyl Glycol	Anatrace	Cat# NG310
Digitonin	Acros Organics	Cat# 11024-24-1
Anti-DYKDDDDK G1 Affinity Resin	GenScript	Cat# L00432
Flag peptide	Sigma-Aldrich	Cat# F3290
Antibiotic Antimycotic Solution	Sigma-Aldrich	Cat# A5955
Lipofectamine 2000 reagent	Thermo Fisher Scientific	Cat#11668027
Cellfectin II reagent	Thermo Fisher Scientific	Cat#10362100
Sf-900™ II SFM medium	Thermo Fisher Scientific	Cat# 10902088
FreeStyle™ 293 Expression Medium	Thermo Fisher Scientific	Cat# 12338018
Critical Commercial Assays		
Superose 6 Increase 10/300 GL	GE healthcare	Cat# 29091596
Deposited Data		
CNGA1/B1 in Apo state	This paper	PDB: 7RH9, EMDB: 24458
CNGA1/B1 in Apo state with CLZ coiled coil	This paper	PDB: 7RHL, EMDB: 24465
cAMP-bound CNGA1/B1 in closed state	This paper	PDB: 7RHG, EMDB: 24460
cGMP-bound CNGA1/B1 in open I state	This paper	PDB: 7RHH, EMDB: 24461
cGMP-bound CNGA1/B1 in open II state	This paper	PDB: 7RHI, EMDB: 24462
L-cis-Diltiazem-blocked CNGA1/B1 in open state	This paper	PDB: 7RHJ, EMDB: 24463
L-cis-Diltiazem-trapped CNGA1/B1 in closed state	This paper	PDB: 7RHK, EMDB: 24464
Experimental Models: Cell Lines		
Sf9 cells	Thermo Fisher Scientific	Cat# 11496015
HEK293F cells	Thermo Fisher Scientific	Cat# R79007; RRID: CVCL_D603
HEK293 cells	ATCC	CRL-1573
Recombinant DNA		
pEZT-BM vector	Morales-Perez et al., 2016	Plasmid # 74099 (Addgene)
pEZT-BM-Flag-CNGA1_B1 and mutations	This paper	N/A
pNGFP-EU	Kawate and Gouaux, 2006	N/A
Software and Algorithms		
MotionCor2	Zheng et al., 2017	http://msg.ucsf.edu/em/software/motioncor2.html
GCTF	Zhang, 2016	https://www.mrc-lmb.cam.ac.uk/kzhang/Gctf/
RELION	Scheres, 2012	http://www2.mrc-lmb.cam.ac.uk/relion

REAGENT or RESOURCE	SOURCE	IDENTIFIER
Chimera	Pettersen et al., 2004	https://www.cgl.ucsf.edu/chimera/
Coot	Emsley et al., 2010	https://www2.mrc-lmb.cam.ac.uk/personal/pemsley/coot
MolProbity	Chen et al., 2010	http://molprobity.biochem.duke.edu/
PyMol	Schrödinger	https://pymol.org/2; RRID:SCR_000305
PHENIX	Adams et al., 2010	https://www.phenix-online.org
HOLE	Smart et al., 1996	http://www.holeprogram.org/
Others		
Quantifoil R1.2/1.3 Au 300 mesh	Electron Microscopy Sciences	Cat# Q3100AR1.3